Precipitation driving of droplet concentration variability in marine low clouds

***Robert Wood[1], David Leon[2], Matthew Lebsock[3], Jefferson Snider[2], Antony D. Clarke[4]**

1. Department of Atmospheric Sciences, 408 ATG Building, University of Washington, Seattle, WA, 98195-1640, USA.

2. Department of Atmospheric Sciences, University of Wyoming, Dept. 3038 1000 E. University Ave., Laramie, WY 82071, USA

3. Jet Propulsion Laboratory, California Institute of Technology, 4800 Oak Grove Drive, Pasadena, California 91109-8099, USA

4. Department of Oceanography, University of Hawai`i at Manoa, 1000 Pope Road, Marine Sciences Building, Honolulu, HI 96822, USA

* Corresponding author (robwood@atmos.washington.edu

Tel: 206-543-1203; Fax: +1 206 685 9302)

June 14th 2012

Abstract

The concentration N_d of cloud droplets in marine low clouds is a primary determinant of their ability to reflect sunlight and modulates their ability to precipitate. Previous studies have focused upon aerosol source variability as the key driver of variability in N_d. Here, we use a highly simplified aerosol budget model to examine the impact of precipitation on N_d. This model considers: precipitation (coalescence) scavenging, constrained using new satellite measurements of light precipitation; entrainment of aerosol from above cloud combined with constant aerosol concentration based on recent field observations of aerosol particles in the free troposphere; and sea-surface aerosol production estimated using a wind-speed dependent source function. Despite the highly simplified nature of this model, it skillfully predicts the geographical variability of N_d in regions of extensive marine low clouds. Inclusion of precipitation results in reduction in N_d by factors of 2-3 over the remote oceans. Within 500 km of coastlines the reduction in N_d due to precipitation is weak but in these regions the model is not able to accurately predict N_d because of strong pollution sources. In general, neither free-tropospheric nor surface CCN sources alone are sufficient to maintain N_d against precipitation losses. The results demonstrate that even the light precipitation rates typical of marine stratocumulus profoundly impact the radiative properties of marine low clouds.

1. Introduction

Anthropogenic activities have resulted in marked increases in the concentration of aerosol particles in the atmosphere [*Kaufman et al.* 2002, *Isaksen et al.* 2009] and these increases exert a significant but highly uncertain radiative forcing on the global climate [*Isaksen et al*. 2009, *IPCC* 2007]. A large fraction of this forcing is attributed to the effects that aerosol particles have on clouds by increasing the concentration N_d of cloud droplets [*Martin et al.* 1994; *Ramanathan et al*. 2001; *Lohmann and Feichter* 2005], reducing droplet size [*Breon et al. 2002*], thereby increasing the reflected solar radiation [*Twomey* 1974, *Penner et al.* 2004, *Quaas et al.* 2009]. Systematic increases in N_d have been observed downwind of east Asia over the past two decades [*Bennartz et al*., 2011] and have been attributed to rapid industrialization. The magnitude of the so-called "aerosol indirect effect" on climate depends not only upon present-day conditions, but also upon the unperturbed microphysical state of the clouds prior to the addition of anthropogenic aerosols [*Platnick and Twomey* 1994, *Oreopoulos and Platnick*, 2008]. It is reasonable to argue that N_d is the single most important cloud microphysical variable that must be accurately represented in models in order to accurately determine aerosol indirect effects on climate. However, there are marked differences between values of N_d in different climate models [*Quaas et al.* 2009, *Ming et al.* 2006, *Gettelman et al.* 2008] demonstrating a clear lack of understanding of the key controls on N_d.

Satellite-based studies use the relationship between observed cloud droplet size or concentration, and nearby clear-sky estimates of aerosol loading, to infer the role that aerosols play in influencing clouds and climate [*Breon et al.* 2002]. Some even go so far as to quantitatively estimate aerosol indirect effects globally [*Quaas et al.* 2008, *Jones et*

70 *al.* 2009]. Inherent in this approach is that correlations between cloud microphysical
71 properties and aerosols in the current climate are indicative of an aerosol influence on
72 cloud properties rather than vice versa. Aerosol-cloud correlative studies do not take the
73 possible effects of precipitation into account. One can make a reasonable case that
74 precipitation-induced aerosol changes will not significantly impact the inferences drawn
75 from these studies only if one assumes that the impacts of precipitation are localized,
76 intermittent, and relatively rare, and that the aerosol fields that interact with the majority
77 of clouds are not significantly affected by precipitation. However, recent observations
78 from the sensitive spaceborne radar on the CloudSat satellite are finding that precipitation
79 occurs more frequently over the globe than previously thought [*Leon et al.* 2008, *Haynes*
80 *et al.* 2009] prompting an examination of the role of precipitation in driving aerosol
81 variability.

82 In this study we use these state-of-the-art quantitative estimates of light
83 precipitation from CloudSat to constrain a simple budget model that predicts the mean
84 concentrations of cloud condensation nuclei (CCN) and cloud droplets over those parts of
85 the global oceans containing extensive low clouds. These clouds are confined within the
86 marine boundary layer (MBL) and are among the most susceptible to aerosol
87 perturbations [*Oreopoulos and Platnick*, 2008]. We build upon previous studies [*Baker*
88 *and Charlson* 1990, *Baker et al.* 1993] that used simplified budget models to provide
89 important insights into the factors controlling CCN, by constructing a steady-state budget
90 for CCN in the MBL appropriate for the regions of large-scale subsidence where
91 extensive marine stratocumulus clouds are favored [*Klein and Hartmann*, 1993].

This article is organized as follows. Section 2 describes the basis for a simple, single-equation, steady-state budget model to predict CCN or N_d in the MBL. Section 3 describes how we determine the terms in the budget using a variety of observations including satellites and in-situ data. Section 4 presents the key results from the model and compares the model against satellite observations of N_d. Section 5 discusses the implications of our findings.

2. Steady state budget model

The rate of increase of CCN concentration $\dot{N}$ averaged over the depth of the MBL can be written as the sum of various source and sink terms:

$$\dot{N} = \dot{N}_{FT} + \dot{N}_S + \dot{N}_{PROD} + \dot{N}_P + \dot{N}_{DRY} + \dot{N}_{ADV} \quad [1]$$

where $\dot{N}_{FT}$, $\dot{N}_S$, $\dot{N}_{PROD}$, $\dot{N}_P$, $\dot{N}_{DRY}$ and $\dot{N}_{ADV}$ are the time tendencies due to entrainment of CCN from the free-troposphere (FT), primary production at the surface (i.e. sea spray), and secondary production, precipitation (i.e. coalescence scavenging), dry deposition to the surface and horizontal advection, respectively.

Free-tropospheric air is constantly being mixed into the MBL by cloud top entrainment, and this can either provide a net source of CCN to the MBL or can dilute MBL aerosol concentrations. Modeling and observational studies suggest that the FT is a primary source of CCN in the remote MBL [*Clarke et al.* 1998b, *Capaldo et al.* 1999, *Katoshevski et al*. 1999]. The net source rate is $\dot{N}_{FT} = w_e(N_{FT}–N)/z_i$ where z_i is the depth of the MBL and w_e is the entrainment rate.

The modeled surface source $\dot{N}_S$ is assumed to be from primary production of sea-spray aerosol (SSA) and we use a recent parameterization [*Clarke et al.* 2006] to provide

$\dot{N}_S = F(\sigma) U_{10}^{3.41} / z_i$ where U_{10} is the wind speed at a height of 10 m, and $F(\sigma)$ depends upon the assumed peak supersaturation σ experienced in the clouds (see section 3.1 below). We examine the sensitivity to the parameterization of sea-spray by comparing with the frequently-used formulation of *Monahan et al.* [1986]. Since this formulation has the same wind speed dependence as *Clarke et al.* [2006], the expression for $\dot{N}_S$ given above is identical for the two schemes, but the function $F(\sigma)$is different. We discuss how the supersaturation and $F(\sigma)$ are specified in Sections 3.1 and 3.3 below.

The model does not take into account CCN formation from the nucleation of new particles in the MBL since it is unlikely that this contributes significantly to the mean CCN number concentration over the oceans. In severely-scavenged ultraclean MBLs evidence of new particle formation has been noted [*Clarke et al.* 1998*, Petters et al.* 2006*, Tomlinson et al.* 2007*, Wood et al.* 2008] . Such nucleation events appear to be quite rare, with only one clear instance observed during four weeks of shipborne sampling over the tropical southeastern Pacific ocean [*Tomlinson et al.* 2007]. In addition, evidence that freshly nucleated particles can grow to sufficient sizes to increase the population of CCN without being scavenged by existing cloud is lacking. Nucleation events are therefore unlikely to compete with other source processes in determining the mean state [*Capaldo et al.* 1999, *Katoshevski et al*. 1999]. In any case, formulations for the rate of production of CCN from new particle formation in the MBL are highly uncertain [*Capaldo et al.* 1999, *Kirkby et al.* 2011]. To maintain simplicity, and because the production rates are highly uncertain, we do not include production of CCN from other secondary processes like aqueous phase processing. We therefore set the secondary production rate $\dot{N}_{PROD} = 0$.

138 The precipitation sink term $\dot{N}_P$ depends upon the precipitation rate at cloud base
139 P_{CB}. We use a formulation that accounts for losses from the collection of cloud droplets
140 by precipitation drops in the cloud via accretion [*Wood* 2006]. This gives $\dot{N}_P = K\,N\,P_{CB}$
141 h/z_i, where $K = 2.25$ m^2 kg^{-1} is a constant that depends upon the collection efficiency of
142 cloud droplets by drizzle drops [*Wood* 2006], and h is the cloud thickness.
143 Dry deposition of CCN to the ocean is estimated using deposition velocity
144 parameterization [*Georgi* 1988] for accumulation mode particles (0.05-1 μm diameter)
145 that make up the bulk of the CCN in the MBL. Rates are in the range 0.001-0.01 cm s^{-1}
146 with the higher values occurring at higher wind speeds and for the larger of the
147 accumulation mode particles. Given these deposition velocities, we find that dry
148 deposition constitutes only a very weak sink for CCN under most circumstances, with
149 loss rates unlikely to exceed 2 cm^{-3} d^{-1} for most values of N observed, and most wind
150 speeds, over the oceans. We are therefore justified in setting $\dot{N}_{DRY} = 0$ in the budget
151 model.
152 We also set $\dot{N}_{ADV} = 0$ to avoid the complication of calculating spatial gradients
153 and to facilitate the interpretation of the key physical processes controlling N_d. It is
154 possible to estimate the magnitude of the advection term $\dot{N}_{ADV}$ using the observed cloud
155 droplet concentration from satellite [*George and Wood* 2010]. Over the remote oceans
156 the magnitude of $\dot{N}_{ADV}$ is generally 10 cm^{-3} d^{-1} or less, while higher values can be found
157 in near-coastal regions. Including advection in the steady state model introduces an
158 additional level of complexity since it involves taking spatial gradients. To preserve
159 simplicity we omit it from the model. Since precipitation is the dominant control on N_d in

160 the model, the geographic pattern of the advection term largely follows the spatial
161 gradient in precipitation rate.

162 In this study we examine the time-mean CCN budget by setting $\dot{N}$=0 in
163 equation (1) inserting the expressions discussed above for the various terms, and
164 rearranging to obtain an expression for the steady-state value N_{eq} of the CCN
165 concentration in the MBL as
166

$$N_{eq} = \frac{\left(N_{FT} + \frac{F(\sigma)U_{10}^{3.41}}{Dz_i}\right)}{\left(1 + \frac{hKP_{CB}}{Dz_i}\right)} \quad [2]$$

167 Here we have also assumed that entrainment is in balance with the large-scale
168 subsidence rate, so that $w_e = D\, z_i$, where D is the large scale divergence, appropriately
169 assumed to be constant with height over the depth of the MBL [*Wood et al.* 2009]. In
170 practice, the entrainment rate exceeds the subsidence rate by 10-40% over the subtropical
171 stratocumulus regions [*Wood and Bretherton* 2004], but estimating its precise value is
172 itself a major challenge [*Stevens* 2002] and is not attempted here.
173

174 **3. Model constraints and inputs**

175 The CCN budget model (equations 1 and 2) implicitly assumes that the cloud
176 droplet concentration N_d and the CCN concentration are one and the same. This is
177 reasonable provided that (a) we choose an appropriate peak supersaturation σ in order to
178 convert the aerosol sources, which are provided as a function of aerosol size, into

179 tendencies of CCN; (b) the cloud droplet concentration throughout the cloud is equal to
180 that determined by the aerosol activation process.
181

182 3.1 Supersaturation

183 For marine stratocumulus clouds, observations suggest that values of σ in the
184 range 0.1-0.8% are typical with mean values around 0.3% consistent with observations
185 [*Martin et al.* 1994, *Snider et al.* 2003]. Here we assume a constant value of σ=0.3% for
186 all calculations. The peak supersaturation σ = 0.3% assumed in the model is assumed to
187 be constant everywhere. Understanding how this changes systematically over the remote
188 oceans is complex, as it depends upon variations in the strength of the turbulent updrafts
189 and upon the size distribution of the aerosol being activated [*Martin et al.* 1994, *Snider et*
190 *al.* 2003]. We use recent field measurements of mean aerosol size distributions at
191 different distances from the Chilean coast from the VOCALS Regional Experiment
192 (REx) [*Wood et al.* 2011] to estimate the likely systematic geographical variability in σ.
193 In the marine boundary layer, the Hoppel minimum [*Hoppel* 1986] in the size distribution
194 is indicative of the minimum size of aerosols that are activated. Assuming a hygroscopic
195 aerosol, this minimum size is directly related to the supersaturation. A systematic
196 reduction from 0.1 to 0.07 μm in the minimum diameter was observed to occur from
197 70°W to 78°W moving westwards along 20°S away from the Chilean coast [*Kleinmann*
198 *et al.* 2012]. This implies that the mean supersaturation increases by ~75% from the coast
199 offshore. However, the coastal CCN concentrations are high consistent with pollution
200 aerosol impacts [*Allen et al.* 2011], and so these are not representative of the

supersaturations we are attempting to represent in the model. No systematic shift in the Hoppel minimum is observed over the cleaner region from 74°W to 78°W, suggesting that systematic changes in supersaturation over the remoter regions may be considerably smaller than occur near the coasts.

3.2 Free-tropospheric CCN

We constrain N_{FT} based on aerosol measurements from field data taken in the Southern and Northern Hemisphere remote subtropical FT. Two data sources are used:

(a) aircraft measurements of FT CCN from a thermal diffusion CCN counter taken on the NSF/NCAR C-130 aircraft during the VOCALS-REx. Details of the instrument are provided in *Snider et al.* (2006), and flight plans are described in *Wood et al.* [2011] A total of 638 CCN measurements were made in the FT (61, 117, 147 and 313 at supersaturations of approximately 0.1, 0.25, 0.5 and 0.9% respectively) along the 20°S latitude line from the coast (70°W) to approximately 1500 km offshore (85°W) over the month-long campaign. CCN concentrations are corrected to an assumed mean MBL pressure of 925 hPa, which is the typical pressure at which clouds form in the region [*Bretherton et al*. 2010];

(b) a composite time-mean size distribution measured over 17 days with large scale subsidence at a remote FT station on Mauna Loa during July 1992. These data are described in *Weber and McMurry* [1996] and are also corrected to a pressure of 925 hPa. We convert the size distribution into a CCN spectrum using a plausible range of aerosol hygroscopicity following the 'kappa' parameter approach [*Petters and Kreidenweis* 2007]. A reasonable lower boundary (κ=0.3) is approximately the lowest value of CCN-based hygroscopicity measured in the

224 northeastern Pacific FT from *Roberts et al.* (2010). The upper boundary (κ=0.98)
225 is the geometric mean value from *Roberts et al.* (2010). Values of κ significantly
226 higher than unity were inferred from CCN measurements in Roberts et al. (2010)
227 but seem implausible given that even the most hygroscopic compounds have κ
228 values of about unity [*Petters and Kreidenweis* 2007]. Ammonium sulfate has a κ
229 value of approximately 0.7 [*Petters and Kreidenweis* 2007].
230
231 Figure 1a compares the measured CCN concentrations in the southeastern Pacific FT
232 with those from Mauna Loa. For the southeastern Pacific, we take data from west of
233 75°W (>500 km off the Chilean coast) that is minimally impacted by coastal pollution
234 [*Allen et al.* 2010]. Time-mean CCN concentrations west of 75°W over the southeastern
235 Pacific Ocean (Fig. 1) are in remarkably good agreement with those derived from the
236 Mauna Loa size distribution measurements. This is perhaps surprising because although
237 the southeastern Pacific and Hawaii are in similar tropical meteorological regimes, one
238 might expect marked differences in the mean size distribution due to the different array of
239 sources and landmasses in the Northern and Southern Hemisphere. The mean
240 distributions are made up of a mixture of different aerosol populations from a number of
241 different sources. Previous studies [*Clarke et al.* 1998b, *Friedlander* 1977, *Raes* 1995]
242 suggest that new particle formation from naturally-produced sulfuric acid in the upper
243 troposphere constitutes one major source of clean FT CCN. This aerosol subsequently
244 subsides in the descending branches of large scale atmospheric systems where its
245 distribution is expected to reach a quasi-steady state [*Friedlander* 1977, *Raes* 1995]. In

addition, the remote marine FT also includes air masses transported long distances from continents that likely contain some pollution aerosol.

We derive a value of N_{FT} in the range 100-175 cm^{-3} active at σ=0.3% from the mean Mauna Loa size distribution (assuming a plausible range of aerosol hygroscopicity, see caption, Fig. 1a). This is in remarkable agreement with mean values from CCN spectrum measurements made in the southern hemisphere subtropical FT during VOCALS-REx (see Fig. 2a). For the model base case we therefore assume a constant mean concentration N_{FT} = 125 cm^{-3} everywhere, which is within 20% of the time-mean values derived from the remote subtropical data in both hemispheres. We also force the model with observed values of FT CCN from VOCALS-REx and conduct additional sensitivity tests, as described in Section 4.

3.3 Sea surface source

For the surface source, we use a size-resolved sea spray generation function [*Clarke et al.* 2006] to estimate the rate of particle generation for particles active at σ=0.3% supersaturation. This is determined numerically by integrating the size-resolved surface source function from the largest particles down to the critical dry diameter for a given supersaturation. This provides a supersaturation-dependent $F(\sigma)$ curve shown in Fig. 1b. For σ=0.3% the critical diameter is 50 nm, which yields a value of 214 m^{-3} $(m\,s^{-1})^{-2.41}$ for σ=0.3% (Fig 1b). For a wind speed of 8 m s^{-1} this yields $\dot{N}_S$ = 22 cm^{-3} d^{-1} averaged over an MBL that is 1 km deep. The widely-used source function of *Monahan et al.* [1986] has the same wind speed dependence but a rate that is over a factor of two lower (Fig. 1b).

To drive SSA production we use daily mean wind speed estimates from the QuikScat satellite and average the production rates up to monthly averages. Including sub-daily timescale variability in wind speed increases the surface production of SSA, but we find from reanalysis data that including 6 hourly estimates increases SSA production by less than 10%.

3.4 Precipitation sink

The model sink term is driven by new precipitation rate estimates from the profiling W-band radar on the CloudSat satellite [*Lebsock and L'Ecuyer* 2011]. The cloud base precipitation rate needed to calculate the coalescence scavenging [*Wood* 2006] is estimated as the maximum value in each radar profile. Mean precipitation rates from low clouds are estimated for 5×5° gridboxes globally by removing profiles with detectable echoes above the 3 km level. For the regions considered, the results are not strongly sensitive to the choice of this level since the majority of the clouds are situated below 2 km. Gridded precipitation rates are produced on a monthly basis for data from 2006-2009.

We also use precipitation measurements from VOCALS-REx to compare against those from CloudSat. For this, we use both aircraft in-situ observations from an optical array probe, and aircraft radar measurements from the University of Wyoming Cloud Radar. The VOCALS-REx precipitation dataset is described in *Bretherton et al.* [2010]. The majority of the aircraft flights were conducted during the later part of the night (03-09 local time) when precipitation rates are at their diurnal maximum.

3.5 Boundary layer depth, cloud thickness, wind speed, and surface divergence.

Equation (2) indicates that we also need to estimate MBL depth z_i, cloud thickness h, surface wind speed U_{10}, and surface divergence D. MBL depth is estimated using from MODIS cloud top temperature retrievals [*Wood and Bretherton* 2004]. Cloud thickness h is estimated with an adiabatic assumption [e.g. *Albrecht et al.* 1990] using MODIS retrievals of cloud liquid water path (LWP). This relationship is $h = (2LWP/\Gamma)^{1/2}$, where Γ is a weak function of temperature and pressure [*Albrecht et al.* 1990], evaluated as described in *Wood and Bretherton* [2004]. Both cloud top temperature and LWP are taken from 1×1° gridded daily Level 3 MODIS products. The results are not strongly sensitive to these parameters. Wind speed and surface divergence estimates are from the QuikScat satellite [see *Wood et al*. 2009 for details].

3.5. Cloud droplet concentration

Satellite estimates of cloud droplet concentration are used to compare against model-derived N_{eq} from Equation (2). Model estimates are produced globally on a 1×1° grid on a month by month basis. Cloud droplet concentration estimates from the Moderate Resolution Imaging Spectroradiometer (MODIS) on the NASA Terra satellite are produced from daily Level 3 data for 1x1° boxes using a visible/near infrared approach [*Bennartz* 2007]. To minimize problems of retrievals in broken clouds, we only include in our averages those daily boxes where the cloud cover from liquid clouds exceeds 0.8. These are then averaged together to provide monthly mean N_d estimates.

313

314 3.6. Model estimates of N_d

315 We use the budget model Equation (2) to predict monthly mean values of N_d by
316 forcing with monthly-mean values of the input variables discussed above. Annual means
317 are then derived from the monthly means only for those months with (a) mean subsidence
318 (positive mean surface divergence); (b) mean boundary layer depth lower than 4 km; and
319 (c) with mean liquid cloud fractions exceeding 0.3. Annual mean data are only analyzed
320 for those locations where at least four months pass the acceptance criteria.

321

322 **4. Results**

323 4.1 Model assessment over the southeastern Pacific

324 To assess the quality of the model, we use recent field measurements from VOCALS-
325 REx that extensively sampled the lower troposphere over the tropical southeastern Pacific
326 Ocean [*Wood et al.* 2011]. The measurements focused upon characterizing the largest
327 semi-permanent subtropical sheet of stratocumulus on Earth that extends westward from
328 the Chilean and Peruvian coasts. Extensive survey sampling was carried out along 20°S
329 from the Chilean coast at 70°W to ~1400 km offshore at 85°W using a combination of
330 different research aircraft. Measurements were made in both the MBL and the lower FT.
331 Figure 2a shows observations of the two key inputs to the budget model, namely the
332 time-mean FT CCN concentration (section 3.2) and the precipitation rate close to the
333 cloud base (section 3.4). CCN concentrations in the FT fall off sharply within 500 km of
334 the coast but, despite considerable day to day variability, the time-mean campaign values

335 remain relatively constant for over 1000 km out to 85°W (Fig 2a). Several lines of
336 evidence point to anthropogenic pollution being responsible for the high values very
337 close to the coast [*Allen et al.* 2011, *Yang et al.* 2011, *Saide et al.* 2012].

338 The cloud base precipitation rate increases markedly with distance from the
339 Chilean coast, from an essentially nonprecipitating state with <0.1 mm d^{-1} near the coast
340 to >1 mm d^{-1} at 85°W (Fig. 2a). Rates of a few tenths of a mm d^{-1} are sufficient to drive
341 significant coalescence scavenging of CCN [*Feingold et al.* 1996, *Wood* 2006]. This
342 gradient in precipitation is driven to a significant extent by thickening clouds and a
343 deeper boundary layer to the west [*Bretherton et al.* 2010], but is likely also modulated
344 by aerosol in the MBL [*Terai et al.* 2012]. The cause of the precipitation is not the focus
345 of this study. Precipitation production in marine stratocumulus maximizes at night [*Leon*
346 *et al.* 2008], and is typically heaviest in the early morning hours when the clouds are at
347 their thickest [*Bretherton et al.* 2004, *Wood et al.,* 2002]. This is apparent in the
348 observations where precipitation rates are lowest at 1:30pm (CloudSat, daytime overpass,
349 Fig. 2a), take intermediate values at 1:30am (CloudSat nighttime overpasss) and are
350 largest during 03-09 am (VOCALS field data). Since the timescale for CCN removal due
351 to precipitation is typically at least 1 day given these precipitation rates [*Wood* 2006], we
352 use a daily mean estimate as the mean of the two CloudSat overpasses to drive the model.

353 The model, when forced with CloudSat observed mean precipitation rates and
354 observed FT CCN, captures the observed increase in N_d as the coast is approached (Fig.
355 2b) with remarkable fidelity given the model's simplicity. The model predicts a factor of
356 two increase in N_d from 90°W to 75°W even when the model is forced with a fixed FT
357 CCN concentration of 125 cm^{-3} (consistent with mean values over the remote region

358 away from the coast). With fixed CCN, however, the model is unable to reproduce the
359 highest concentrations within 500 km of the coast (Fig. 2b). However, these high values
360 are obtained when the model is forced with the observed longitudinally-varying FT CCN
361 concentration increase that includes the near-coastal enhancement due to pollution
362 sources [*Allen et al.* 2011] (Fig 2b). The general behavior of decreasing N_d westward
363 from 75-90°W is caused by increasing precipitation scavenging (Fig. 2a), which can be
364 seen by comparing the model estimates with fixed FT CCN and either no precipitation or
365 precipitation fixed at a constant value of 1 mm d^{-1} (Fig 2b). A critical finding here is that
366 a precipitation rate of as little as 1 mm d^{-1} is sufficient to drive down N_d by a factor of
367 three over the remote ocean, which further serves to emphasize how important
368 precipitation from low clouds is in controlling mean cloud droplet concentrations over the
369 remote ocean.

370 Primary production from sea-spray constitutes a weaker, but nevertheless
371 significant, source than entrainment from the FT consistent with a previous study with the
372 same parameterization [*Clarke et al.* 2006]. However, it is important to note that we are
373 using a source function that is one of the more prolific available [*de Leeuw et al*. 2011],
374 although experimentation with different primary production parameterizations only
375 changes the modeled N_d values by less than 20% (Fig. 3). The CCN concentration from
376 sea-salt (the difference between the solid and the dotted line in Fig. 3) ranges from <10
377 cm^{-3} close to the Chilean coast, where wind speeds are low, to around 40 cm^{-3} further
378 afield, where wind speeds are higher. These findings are consistent with preliminary
379 measurements of sea-salt particles from aircraft during VOCALS-REx (Anthony Clarke,
380 personal communication). The choice of sea-spray parameterization does not affect our

conclusions regarding the importance of precipitation at driving the offshore gradient in cloud droplet concentration over the southeastern Pacific.

4.2 Application to marine low cloud regions globally

Given the ability of the budget model with fixed FT CCN concentrations to reproduce with some skill the gradient in N_d over the remote southeastern Pacific Ocean (more than 500 km from the coast), we apply the model more generally to regions of extensive marine low cloud under conditions of large scale subsidence (Fig. 4). Aerosol concentrations in the FT vary significantly both regionally and in response to variations in natural and anthropogenic sources [*Allen et al.* 2011]. Because there are no global observational constraints on the time-mean FT CCN, we draw on the consistency between mean FT CCN spectra at Mauna Loa and over the southeastern Pacific Ocean (Fig. 1 and section 3.2) and fix $N_{FT} = 125$ cm^{-3} everywhere for the base case. The satellite observations show that N_d values in excess of 150 cm^{-3} tend to be located near the continental coastlines (e.g. California, Chile/Peru, Europe), with values reducing toward the remote oceans, where they are as low as 30-60 cm^{-3} (Fig. 4a). The base case model is able to reproduce well the mean values (Table 1) and geographical variability in N_d (Fig. 4) for low cloud regions, especially for the remote subtropical/tropical regions 35°S-35°N. The model underestimates N_d close to coastlines (Table 1) consistent with a lack of continental sources. The model also captures the low values (<60 cm^{-3}) over the remote North Pacific and Atlantic and the Southern Ocean north of 45°S. Removing the precipitation sink increases mean N_d in the model by a factor of 2-3 over the remote oceans, but only 15% in the near-coastal regions where precipitation rates are very low

(Table 1). A doubling of N_{FT} from 80 to 160 cm^{-3} leads to a 50-70% increase in N_d (Table 1) because FT CCN is partly buffered by surface sources.

The skill of the base case model in predicting N_d variability is remarkable given that there is no variation whatsoever in the FT CCN source in Fig. 4. To examine the key factors controlling the geographical variability of N_d in the model, we conduct additional model sensitivity experiments. In each experiment, only one (or two) of the variables in equation (2) is allowed to vary. All other variables are fixed by setting them to their respective mean values over time and space (Table 2). It is clear that precipitation variability is required in order to produce the strong correlation with observations seen in the base case (r = 0.65). No other variable can alone explain more than 15% of the observed geographical variance in N_d. Divergence and cloud thickness variations also lead to model fields with significant positive correlations (r =0.21 and 0.37 respectively), but the geographical variability in N_d driven by these variables is far too weak to explain the observed variability (Table 2). The correlations are positive because divergence and cloud thickness correlate quite well with precipitation itself. We find that wind speed variability alone explains an insignificant amount of the model N_d variability (r = -0.06), from which we conclude that variability in SSA is not a significant contributor to the observed geographical variability in N_d. This is especially true in the subtropics and tropics where wind speeds are relatively modest and the FT source is greater than the surface source (Fig. 5). However, SSA does contribute to the mean N_d (Table 1) despite not substantially impacting its geographical variability.

Overall, these results lead us to argue that a large fraction of the observed geographical variability in cloud droplet concentration in extensive marine low clouds

over the remote oceans is driven by precipitation losses rather than aerosol source variability. This is further demonstrated by noting the striking similarities between the maps of the mean observed precipitation rates from low clouds (Fig. 6) and the observed N_d field (Fig. 4a).

Frequency distributions of monthly mean N_d (Fig. 7) show that the base case model (N_{FT} = 125 cm^{-3}) can represent satellite-observed N_d variability well. As we might expect from Fig. 2, the model is unable to capture the very highest concentrations observed by the satellite (N_d > 200 cm^{-3}) that are mostly regions within a few hundred kilometers of coastlines. This is because neither the advection of continentally-influenced MBL air nor elevated near-coastal FT concentrations (e.g., Fig. 2) are considered in the model. When the model is forced by removing either FT CCN or SSA production, the model is unable to represent the distribution of observed N_d and underestimates the mean N_d (Fig. 7 and see also Table 1). This further emphasizes that the surface and FT are both important contributors to the cloud droplet concentration over the remote oceans [*Katoshevski et al.* 1999, *Capaldo et al.* 1999, *Clarke et al.* 2006]. The shape of the model N_d distribution is relatively insensitive to plausible variations in the assumed mean FT CCN concentration (Fig. 8).

5. Implications and conclusions

Our results have a number of important implications. First, if CCN and cloud droplet concentration variability over much of the global ocean are determined by precipitation variability rather than aerosol source variability, this calls into question the interpretation of correlative studies [*Quaas et al.* 2008, *Jones et al.* 2009] linking cloud

properties to aerosol properties as providing useful information on anthropogenic aerosol indirect effects on climate. It also suggests that the notion of there being a 'background' aerosol concentration in the unperturbed marine boundary layer may not be a useful one because MBL CCN concentrations are strongly modulated by precipitation processes that vary strongly both geographically and temporally. The FT CCN over remote oceanic regions is known to reflect a complex mixture of different sources, some of which are natural and some anthropogenic [*Clarke and Kapustin 2010*]. Our finding that a constant time-mean FT CCN supply is sufficient to explain a significant fraction of the time-mean gradients in the cloud droplet concentration over the remote oceans should not therefore be interpreted as indicating that the remote oceanic regions are devoid of anthropogenic influence. The increasing concentrations observed within about 500 km of continents most likely reflects a lower tropospheric pathway for the transport of continental aerosols to the MBL, whereas the more remote anthropogenic contributions are associated with aerosol or precursors lofted higher into the troposphere that can then be transported long distances before subsidence carries them into the MBL.

Here we have shown that MBL cloud droplet concentrations are impacted by precipitation generated by the clouds themselves, but we note that an increasing body of evidence shows that precipitation in low clouds typically decreases with cloud droplet concentration [*Stevens and Feingold* 2009]. There is then the potential for a significant positive feedback whereby modest increases in CCN reduce the precipitation sink, amplifying the initial perturbation. Although we do not claim evidence for bistability in the system [*Baker and Charlson* 1990], our results do suggest that pollution-driven CCN increases may be amplified by precipitation suppression and that this warrants further

exploration with more sophisticated models. There is modeling evidence for this in the recent literature [*Yang et al.* 2012].

Finally, we note that climate models tend to impose arbitrary fixed limits on cloud droplet concentration minima [*Quaas et al.* 2009] suggesting deficiencies in modeling the processes responsible for low concentrations over the remote ocean. Across models, there is a significant correlation between this fixed lower limit on N_d and the strength of the aerosol indirect effect [*Quaas et al.* 2009]. A closer focus on the role of precipitation is therefore needed to better understand whether climate models are able to produce light precipitation in the marine boundary layer, and whether the models are impacted appropriately by it. This study helps to highlight that we now have the satellite measurements of light precipitation and cloud microphysical properties to begin to explore this critical control on cloud microphysical properties. Further work could include an examination of the effects of seasonal precipitation variability on the seasonal cycle of cloud droplet concentration, as suggested by previous work [Liu 2010].

Acknowledgements:

The authors would like to thank the staff and crew of the NSF/NCAR C-130 aircraft whose dedication resulted in the in-situ observational VOCALS Regional Experiment dataset. The CloudSat data were distributed by the CloudSat Data Processing Center at Colorado State University. MODIS data were obtained from the NASA Goddard Land Processes data archive. QuikScat data were produced by Remote Sensing Systems and sponsored by the NASA Ocean Vector Winds Science Team. This work was supported by NASA award numbers NNX10AN78G and NNX10AM29G and NSF award numbers ATM-0745702 and ATM-0745368.

References

Albrecht, B. A., C. W. Fairall, D. W. Thomson, A. B. White, J. B. Snider, and W. H. Schubert, 1990: Surface-based remote-sensing of the observed and the adiabatic liquid water content of stratocumulus clouds. *Geophys. Res. Lett.*, 17, 89–92.

Allen, G., Coe, H., Clarke, A., Bretherton, C., Wood, R., Abel, S. J., Barrett, P., Brown, P., George, R., Freitag, S., McNaughton, C., Howell, S., Shank, L., Kapustin, V., Brekhovskikh, V., Kleinman, L., Lee, Y.-N., Springston, S., Toniazzo, T., Krejci, R., Fochesatto, J., Shaw, G., Krecl, P., Brooks, B., McMeeking, G., Bower, K. N., Williams, P. I., Crosier, J., Crawford, I., Connolly, P., Allan, J. D., Covert, D., Bandy, A. R., Russell, L. M., Trembath, J., Bart, M., McQuaid, J. B., Wang, J., and Chand, D.: South East Pacific atmospheric composition and variability sampled along 20° S during VOCALS-REx, Atmos. Chem. Phys., 11, 5237-5262, doi:10.5194/acp-11-5237-2011 (2011).

Baker, M. B., and R. L. Charlson. Bistability of CCN concentrations and thermodynamics in the cloud-topped boundary layer. *Nature,* **345,** 142–145 (1990).

Baker, M. B. Variability in concentrations of cloud condensation nuclei in the marine cloud-topped boundary layer. *Tellus,* **45B,** 458–472 (1993).

Bennartz, R. Global assessment of marine boundary layer cloud droplet number concentration from satellite, J. Geophys. Res., 112, D02201 (2007).

Bennartz, R., J. Fan, J. Rausch, L. R. Leung, and A. K. Heidinger. Pollution from China increases cloud droplet number, suppresses rain over the East China Sea, Geophys. Res. Lett., 38, L09704, doi:10.1029/2011GL047235 (2011).

Bréon, F. M., Tanre, D., Generoso, S. Aerosol effect on cloud droplet size monitored from satellite. *Science*, **295,** 834-838 (2002).

Bretherton, C. S., Wood, R., George, R. C., Leon, D., Allen, G., and Zheng, X.: Southeast Pacific stratocumulus clouds, precipitation and boundary layer structure sampled along 20°S during VOCALS-REx, *Atmos. Chem. Phys.*, **10**, 10639-10654 (2010).

528 Capaldo K. P., Kasibhatla P., and Pandis S.N. Is aerosol production within the remote
529 marine boundary layer sufficient to maintain observed concentrations? *J. Geophys.*
530 *Res.*,**104**, 3483-3500 (1999).

531 Clarke, A. D., et al., Particle nucleation in the tropical boundary layer and its coupling to
532 marine sulfur sources, Science, 282, 89– 92 (1998a).

533 Clarke, A. D., J. L. Varner, F. Eisele, R. L. Mauldin, D. Tanner, and M. Litchy. Particle
534 production in the remote marine atmosphere: Cloud outflow and subsidence during
535 ACE 1, *J. Geophys. Res.*, 103(D13), 16,397–16,409 (1998b).

536 Clarke, A. D., S. R. Owens, and J. Zhou. An ultrafine sea-salt flux from breaking waves:
537 Implications for cloud condensation nuclei in the remote marine atmosphere, *J.*
538 *Geophys. Res*., **111**, D06202 (2006).

539 Clarke, A. D., and Kapustin, V.: Hemispheric aerosol vertical profiles: anthropogenic
540 impacts on optical depth and cloud nuclei, *Science*, **329**, 1488–1492, (2010)

541 de Leeuw, G., E. L Andreas, M. D. Anguelova, C. W. Fairall, E. R. Lewis, C. O'Dowd,
542 M. Schulz, and S. E. Schwartz: Production flux of sea spray aerosol, *Rev. Geophys*.,
543 **49**, RG2001 (2011).

544 Feingold, G., S. M. Kreidenweis, B. Stevens, and W. R. Cotton. Numerical simulations of
545 stratocumulus processing of cloud condensation nuclei through collision-coalescence,
546 J. Geophys. Res., 101, 21,391–21,402 (1996).

547 Friedlander, S.K. *Smoke, dust and haze*. John Wiley and Sons (1977).

548 George, R. C. and Wood, R. Subseasonal variability of low cloud radiative properties
549 over the southeast Pacific Ocean, *Atmos. Chem. Phys*., **10**, 4047-4063,
550 doi:10.5194/acp-10-4047-2010 (2010).

551 Gettelman, A., H. Morrison, S. J. Ghan. A New Two-Moment Bulk Stratiform Cloud
552 Microphysics Scheme in the Community Atmosphere Model, Version 3 (CAM3).
553 Part II: Single-Column and Global Results. *J. Climate*, **21**, 3660–3679 (2008).

554 Giorgi, F. Dry deposition velocities of atmospheric aerosols as inferred by applying a
555 particle dry deposition parameterization to a general circulation model. *Tellus B*, **40B**,
556 23-41 (1988).
557
558 Haynes, J. M., T. S. L'Ecuyer, G. L. Stephens, S. D. Miller, C. Mitrescu, N. B. Wood,
559 and S. Tanelli. Rainfall retrieval over the ocean with spaceborne W-band radar, J.
560 Geophys. Res., 114, D00A22, (2009).
561 Hoppel, W. A., Frick, G. M., and Larson, R. E.: Effects of nonprecipitating clouds on the
562 aerosol size distribution in the marine boundary layer, Geophys. Res. Lett., 13, 125–
563 128, 1986.
564 IPCC, 2007. Climate Change: The Physical Science Basis. Contribution of Working
565 Group I to the Fourth Assessment Report of the Intergovernmental Panel on Climate
566 Change. S. Solomon, D. Qin, M. Manning, Z. Chen, M. Marquis, K.B. Averyt,
567 M.Tignor and H.L. Miller (eds.) Cambridge University Press, Cambridge, United
568 Kingdom and New York, NY, USA (2007).
569 Isaksen, I. S. A. et al. Atmospheric composition change: Climate–Chemistry interactions.
570 *Atmospheric Environment*, **43**, 5138-5192 (2009).
571 Jones, T. A., Christopher, S. A., and Quaas, J. A six year satellite-based assessment of the
572 regional variations in aerosol indirect effects, *Atmos. Chem. Phys.*, **9**, 4091-4114,
573 (2009).
574 Katoshevski, D., Nenes, A., and Seinfeld, J. H. A Study of processes that govern the
575 maintenance of aerosols in the marine boundary layer, *J. Aerosol Sci.*, **30**, 503-532
576 (1999).
577 Kaufman, Y., D. Tanré, and O. Boucher. A satellite view of aerosols in the climate
578 system. *Nature*, **419**, 215-223 (2002).
579 Kirkby, J., et al., Role of sulphuric acid, ammonia and galactic cosmic rays in
580 atmospheric aerosol nucleation. *Nature*, **476**, 429-433 (2011).

581 Klein, S. A. and D. L. Hartmann. The seasonal cycle of low stratiform clouds. *J.*
582 *Climate*,, 6, 1588–1606 (1993).

583 Kleinman, L. I., Daum, P. H., Lee, Y.-N., Lewis, E. R., Sedlacek III, A. J., Senum, G. I.,
584 Springston, S. R., Wang, J., Hubbe, J., Jayne, J., Min, Q., Yum, S. S., and Allen, G.:
585 Aerosol concentration and size distribution measured below, in, and above cloud
586 from the DOE G-1 during VOCALS-REx, Atmos. Chem. Phys., 12, 207-223,
587 doi:10.5194/acp-12-207-2012, 2012.

588 Lebsock, M. D., and T. S. L'Ecuyer, The retrieval of warm rain from CloudSat, *J.*
589 *Geophys. Res*., doi:10.1029/2011JD016076 (2011).

590 Leon, D. C., Z. Wang, and D. Liu. Climatology of drizzle in marine boundary layer
591 clouds based on 1 year of data from CloudSat and Cloud-Aerosol Lidar and Infrared
592 Pathfinder Satellite Observations (CALIPSO), J. Geophys. Res., 113, D00A14
593 (2008).

594 Yangang Liu. (2010) Comments on "Seasonal Variation of the Physical Properties of
595 Marine Boundary Layer Clouds off the California Coast". *Journal of Climate* **23**:12,
596 3416-3420.

597 Lohmann, U., and J. Feichter. Global indirect aerosol effects: a review. *Atmos. Chem.*
598 *Phys. Disc.* 5, 715–737 (2005).

599 Martin, G. M., D. W. Johnson, and A. Spice. The measurement and parameterization of
600 effective radius of droplets in warm stratocumulus clouds. *J. Atmos. Sci.*, 51, 1823–
601 1842 (2004).

602 Ming, Y, V. Ramaswamy, L. J Donner, and V. T. J. Phillips. A new parameterization of
603 cloud droplet activation applicable to general circulation models**.** *J. Atmos. Sci..*, **63**,
604 DOI:10.1175/JAS3686.1 (2006).

605 Monahan, E. C., D. E. Spiel, and K. L. Davidson (1986), A model of marine aerosol
606 generation via whitecaps and wave disruption, in Oceanic Whitecaps and Their Role
607 in Air-Sea Exchange Processes, edited by E. C. Monahan and G. Mac Niocaill, pp.
608 167– 193, Springer, New York.

609 Oreopoulos L., and S. Platnick. The radiative susceptibility of cloudy atmospheres to
610 droplet number perturbations: 2. Global analysis from MODIS *J. Geophys. Res.*, **113**,
611 D14S21 (2008).

612 Penner, J. E., X. Q. Dong, and Y. Chen. Observational evidence of a change in radiative
613 forcing due to the indirect aerosol effect. *Nature*., **427**, 231-234 (2004).

614 Petters, M. D. and Kreidenweis, S. M.: A single parameter representation of hygroscopic
615 growth and cloud condensation nucleus activity, Atmos. Chem. Phys., 7, 1961-1971,
616 doi:10.5194/acp-7-1961-2007, 2007.

617 Platnick, S., and S. Twomey, 1994: Determining the susceptibility of cloud albedo to\
618 changes in droplet concentrations with the advanced very high resolution radiometer.
619 *J. Appl. Meteorol*., **33**, 334-347.

620 Quaas, J., O. Boucher, N. Bellouin, and S. Kinne. Satellite-based estimate of the direct
621 and indirect aerosol climate forcing, *J. Geophys. Res.*, 113, D05204,
622 doi:10.1029/2007JD008962 (2008).

623 Quaas, J et al. Aerosol indirect effects – general circulation model intercomparison and
624 evaluation with satellite data, *Atmos. Chem. Phys*., **9**, 8697-8717 (2009).

625 Ramanathan, V., P. J. Crutzen, J. T. Kiehl, and D. Rosenfeld. Aerosols, climate, and the
626 hydrological cycle. *Science*. **294**, 2119-2124 (2001).

627 Roberts, G. C., Day, D. A., Russell, L. M., Dunlea, E. J., Jimenez, J. L.,
628 Tomlinson, J. M., Collins, D. R., Shinozuka, Y., and Clarke, A. D.: Characterization
629 of particle cloud droplet activity and composition in the free troposphere and the
630 boundary layer during INTEX-B, Atmos. Chem. Phys., 10, 6627-6644,
631 doi:10.5194/acp-10-6627-2010, 2010.

632 Saide, P. E., Spak, S. N., Carmichael, G. R., Mena-Carrasco, M. A., Yang, Q., Howell,
633 S., Leon, D. C., Snider, J. R., Bandy, A. R., Collett, J. L., Benedict, K. B., de Szoeke,
634 S. P., Hawkins, L. N., Allen, G., Crawford, I., Crosier, J., and Springston, S. R.:
635 Evaluating WRF-Chem aerosol indirect effects in Southeast Pacific marine
636 stratocumulus during VOCALS-REx, Atmos. Chem. Phys., 12, 3045-3064,
637 doi:10.5194/acp-12-3045-2012, 2012

638 Snider, J. R., M. D. Petters, P. Wechsler and P. Liu, Supersaturation in the Wyoming
639 CCN instrument, *J. Atmos. Oceanic Technol.*, 23, 1323-1339, 2006.

640 Twomey, S., 1974: Pollution and the planetary albedo. *Atmos. Env.*, 8, 1251–1256.

641 Petters, M. D., J. R. Snider, B. Stevens, G. Vali, I. Faloona, and L. M. Russell (2006),
642 Accumulation mode aerosol, pockets of open cells, and particle nucleation in the
643 remote subtropical Pacific marine boundary layer, J. Geophys. Res., 111, D02206,
644 doi:10.1029/2004JD005694.

645 Raes, F. Entrainment of free tropospheric aerosols as a regulating mechanism for cloud
646 condensation nuclei in the remote marine boundary layer, *J. Geophys. Res.*, **100**,
647 2893–2903 (1995).

648 Snider, J. R., S. Guibert, J. L. Brenguier, and J. P. Putaud. Aerosol activation in marine
649 stratocumulus clouds: 2. Kohler and parcel theory closure studies. *J. Geophys. Res.,*
650 **108**, 8629 (2003).

651 Stevens, B. Entrainment in stratocumulus-topped mixed layers. *Quarterly Journal of the*
652 *Royal Meteorological Society* **128**, 2663–2690 (2002).

653 Stevens, B., and G. Feingold. Untangling aerosol effects on clouds and precipitation in a
654 buffered system. *Nature*, **461**, doi:10.1038/nature08281 (2009).

655 Terai, C. R., Wood, R., Leon, D. C., and Zuidema, P.: Does precipitation susceptibility
656 vary with increasing cloud thickness in marine stratocumulus?, *Atmos. Chem. Phys.*,
657 12, 4567-4583, doi:10.5194/acp-12-4567-2012, 2012.

658 Tomlinson, J. M., R. Li, and D. R. Collins. Physical and chemical properties of the
659 aerosol within the southeastern Pacific marine boundary layer, J. Geophys. Res., 112,
660 D12211 (2007).

661 Weber, R. J. and P. H. McMurry. Fine particle size distribution measurements at Mauna
662 Loa Observatory, Hawaii, *J. Geophys. Res.*, **101**, 14767-14775 (1996).

663 Wood, R., C. S. Bretherton, and D. L. Hartmann. Diurnal cycle of liquid water path over
664 the subtropical and tropical oceans. *Geophys. Res. Lett.* **10**.1029/2002GL015371
665 (2002).

Wood, R., and C.S. Bretherton. Boundary layer depth, entrainment and decoupling in the cloud-capped subtropical and tropical marine boundary layer. *J. Clim.* 17, 3576–3588 (2004).

Wood, R., The rate of loss of cloud droplets by coalescence in warm clouds. *J.Geophys. Res*., **111**, D21205 (2006).

Wood, R., K. K. Comstock, C. S. Bretherton, C. Cornish, J. Tomlinson, D. R. Collins, and C. Fairall. Open cellular structure in marine stratocumulus sheets, *J. Geophys. Res.*, 113, D12207 (2008).

Wood, R., M. Köhler, R. Bennartz, C. O'Dell. The diurnal cycle of surface divergence over the global oceans. *Quart. J. Roy. Meteorol. Soc*., **135,** 1484-1493 (2009).

Wood, R. et al. The VAMOS Ocean-Cloud-Atmosphere-Land Study Regional Experiment (VOCALS-REx): goals, platforms, and field operations, *Atmos. Chem. Phys*., **11**, 627-654 (2011).

Yang, Q., W. I. Gustafson Jr., Fast, J. D., Wang, H., Easter, R. C., Morrison, H., Lee, Y.-N., Chapman, E. G., Spak, S. N., and Mena-Carrasco, M. A.: Assessing regional scale predictions of aerosols, marine stratocumulus, and their interactions during VOCALS-REx using WRF-Chem, Atmos. Chem. Phys., 11, 11951-11975, doi:10.5194/acp-11-11951-2011, 2011.

686 **Figure Captions**
687
688 **Figure 1: (a) Free-tropospheric CCN spectra from the southeastern Pacific and**
689 **Hawaii.** Observations from the southeastern Pacific are from CCN spectra taken in the
690 remote FT west of 75°W using the NSF/NCAR C-130 aircraft in VOCALS-REx [*Wood*
691 *et al.* 2011], corrected to an assumed mean MBL pressure of 925 hPa. Box-whisker plots
692 show the 10^{th}, 25^{th}, 50^{th} , 75^{th}, and 90^{th} percentile concentrations for four supersaturations.
693 Shaded region shows a plausible range of CCN concentration estimated using the
694 composite size distribution for subsiding FT air measured on Mauna Loa in Hawaii
695 [*Weber and McMurry* 1996], corrected to an assumed mean MBL pressure of 925 hPa,
696 with the spread representing a plausible range of hygroscopicity κ parameters [*Petters*
697 *and Kreidenweis* 2007] for clean FT air (see text); **(b) Sea-spray source functions** $F(\sigma)$
698 as a function of supersaturation, for the Clarke et al. (2006) parameterization used in this
699 study, and from Monahan et al. (1986) for comparison.
700
701 **Figure 2: Model inputs and results from southeastern Pacific stratocumulus region**
702 **from 70-90°W along 20°S. (a)** Free-tropospheric (FT) aerosol concentrations (left axis)
703 showing range of mean CCN concentrations corresponding to supersaturations relevant
704 for cloud formation (gray shading), and total non-volatile particle concentration (open
705 circles). Green bar shows estimated CCN for 0.2-0.5% supersaturation from
706 measurements of FT aerosol size distributions during subsiding conditions on Mauna
707 Loa, Hawaii, see the Methods section; cloud base precipitation rates (right axis) estimated
708 from CloudSat satellite (mean for October/November 2006-2009 between 22°S and 18°S,
709 red shading showing 1:30am and 1:30pm local time overpasses) and from the VOCALS-
710 REx field experiment (black and blue squares from aircraft radar and in-situ precipitation
711 probes respectively, in the latitude range 18-22°S); **(b)** observed (solid circles: aircraft
712 during VOCALS [*Bretherton et al.* 2010, *Wood et al.* 2011], diamonds: satellite estimates
713 from MODIS, 18-22°S) and modeled mean cloud droplet concentration N_d for different
714 model scenarios as denoted in legend and discussed in the text.
715
716 **Figure 3: Effects of different assumptions regarding primary production of sea-salt**
717 **in the model.** Same as Fig. 2b, but showing sensitivity to sea-salt aerosol
718 parameterization used. Observed (solid circles: aircraft during VOCALS [taken from
719 *Bretherton et al.* 2010], diamonds: satellite estimates from MODIS, 18-22°S) and
720 modeled mean cloud droplet concentration N_d. Solid line: standard model set up with
721 constant FT CCN. Dashed line: Monahan sea-salt parameterization [*Monahan et al.*
722 1986] in place of *Clarke et al.* [2006]. Dotted line: No primary production of sea-salt at
723 all.
724 **Figure 4: Cloud droplet concentrations in regions of extensive marine low clouds**
725 **observed by satellite and from the budget model.** Annual mean cloud droplet
726 concentration N_d for extensive marine low clouds under conditions of large scale
727 subsidence, (a) from MODIS (see Methods section); (b) from the CCN budget model for
728 the same regions.
729
730 **Figure 5: Mean precipitation rate at cloud base from low clouds (cloud top height**
731 **z_{top}<3 km) estimated with spaceborne radar measurements from CloudSat** [Lebsock

and L'Ecuyer 2011]**.** Data are screened to display regions of extensive marine low clouds under conditions of mean subsidence as in Fig. 4.

Figure 6: Ratio of CCN flux from surface to that from entrainment from the free troposphere (FT) in the model. The FT CCN concentration is set to 125 cm^{-3} and the surface source depends upon daily wind speed. In the subtropics and tropics, the majority of the CCN originate from the FT, but in the midlatitudes where winds are stronger, the surface source can exceed that from the FT.

Figure 7: Frequency distributions of observed and modeled monthly mean cloud droplet concentration. Only months that meet the criteria needed to contribute to the means shown in Fig. 4 (regions with extensive low clouds under divergent conditions) are shown. Shown here are the base version of the model (i.e. that used to construct Fig. 4, solid black), together with estimates with no FT contribution to CCN (dashed), and no sea salt contribution (dotted). Error bars show the 95% confidence interval in the frequency estimates for the observations and for the model base case due to sampling limitations.

Figure 8: Sensitivity to assumed free tropospheric CCN concentration N_{FT} of the frequency distributions modeled monthly mean cloud droplet concentration. Only months that meet the criteria needed to contribute to the means shown in Fig. 4 (regions with extensive low clouds under divergent conditions) are shown. Shown here are the base version of the model (i.e. that used to construct Fig. 4, solid black), together with model estimates with low (N_{FT} = 80 cm^{-3}) and high (N_{FT} = 160 cm^{-3}) estimates of the FT contribution to CCN (dashed blue and orange respectively). Error bars show the 95% confidence interval in the frequency estimates for the observations and for the model base case due to sampling limitations.

TABLES

Table 1: The effects on the mean cloud droplet concentration in various geographical regions of changing the primary source and sink terms

Observed or model estimate	Mean cloud droplet concentration [cm^{-3}]		
	35°S-35°N	35°S-35°N within 300 km of coastlines	60°S-60°N
Observations (MODIS)	**88**	**152**	**74**
Model, base case (N_{FT} = 125 cm^{-3})	88	129	74
Model, N_{FT} = 0	20	21	25
Model, no SSA	68	109	46
Model, no precipitation	169	150	245
Model, N_{FT} = 80 cm^{-3}	63	90	55
Model, N_{FT} = 160 cm^{-3}	107	154	85

Table 2: Geographical variability of cloud droplet concentration for various model configurations. Results show correlation coefficients between annual mean MODIS observed and model estimates of annual mean N_d and the ratio of the model and observed standard deviations ($\sigma_{model}/\sigma_{obs}$). Correlations not significant at the 2σ level are italicized. All results are for the tropics and subtropics (35°S-35°N).

Model configuration	r (obs, model)	$\sigma_{model}/\sigma_{obs}$
Base case	0.65	0.92
P_{CB} variability only	0.77	1.01
P_{CB} and U_{10} variability only	0.70	0.97
U_{10} variability only	*-0.06*	0.37
D variability only	0.21	0.18
h variability only	0.37	0.13
z_i variability only	-0.32	0.10

FIGURES

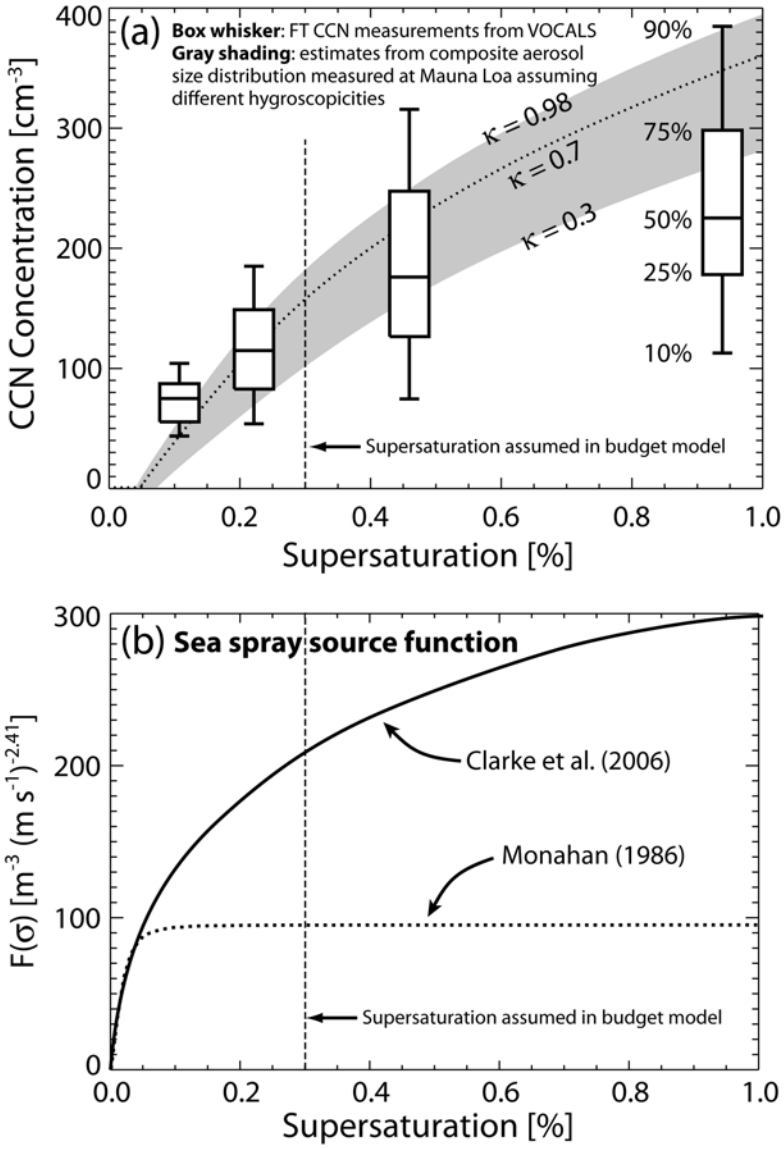

Figure 1: (a) Free-tropospheric CCN spectra from the southeastern Pacific and Hawaii. Observations from the southeastern Pacific are from CCN spectra taken in the remote FT west of 75°W using the NSF/NCAR C-130 aircraft in VOCALS-REx [*Wood et al.* 2011], corrected to an assumed mean MBL pressure of 925 hPa. Box-whisker plots show the 10th, 25th, 50th , 75th, and 90th percentile concentrations for four supersaturations. Shaded region shows a plausible range of CCN concentration estimated using the composite size distribution for subsiding FT air measured on Mauna Loa in Hawaii [*Weber and McMurry* 1996], corrected to an assumed mean MBL pressure of 925 hPa, with the spread representing a plausible range of hygroscopicity κ parameters [*Petters and Kreidenweis* 2007] for clean FT air (see text); **(b) Sea-spray source functions** $F(\sigma)$ as a function of supersaturation, for the Clarke et al. (2006) parameterization used in this study, and from Monahan et al. (1986) for comparison.

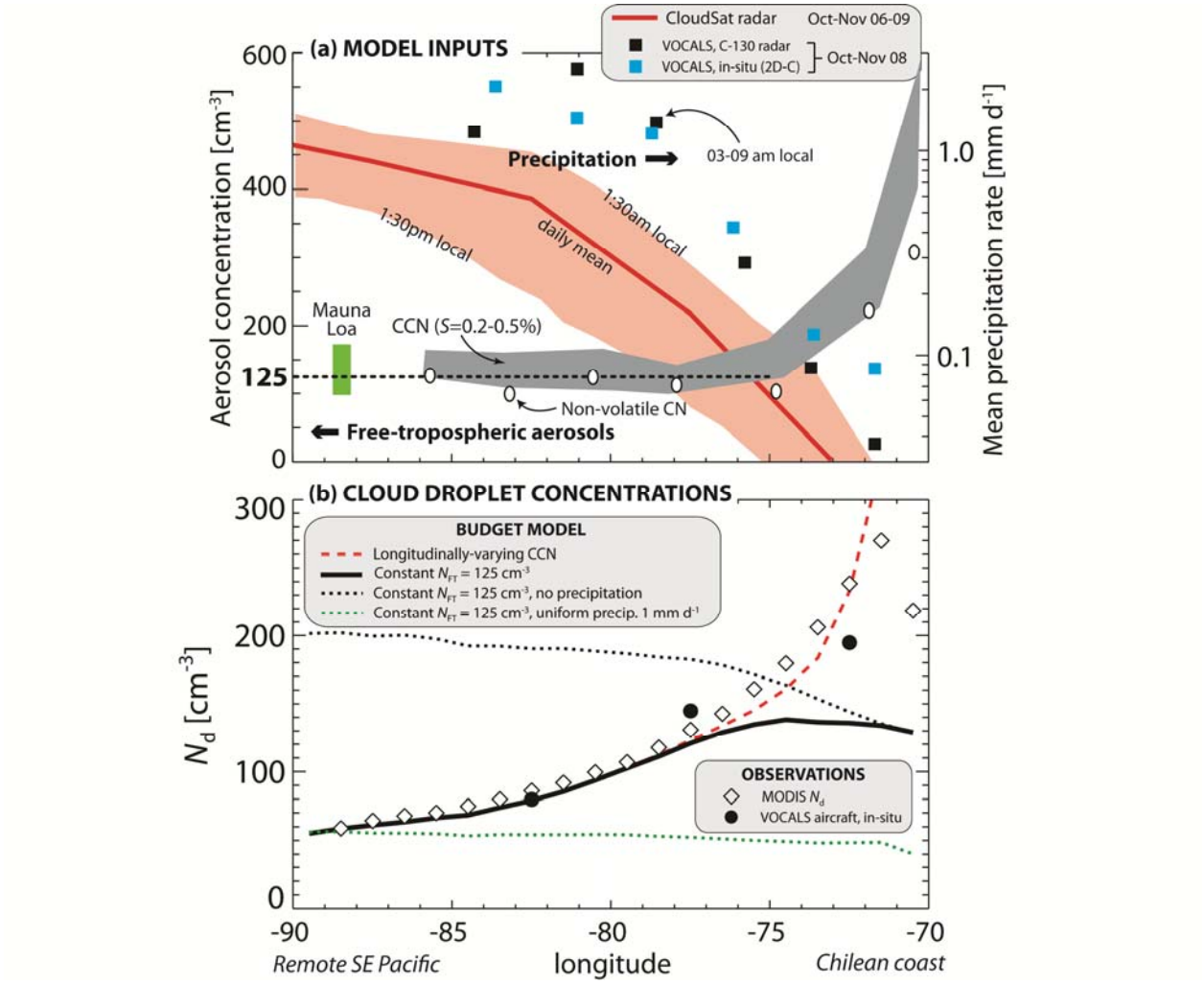

Figure 2: Model inputs and results from southeastern Pacific stratocumulus region from 70-90°W along 20°S. (a) Free-tropospheric (FT) aerosol concentrations (left axis) showing range of mean CCN concentrations corresponding to supersaturations relevant for cloud formation (gray shading), and total non-volatile particle concentration (open circles). Green bar shows estimated CCN for 0.2-0.5% supersaturation from measurements of FT aerosol size distributions during subsiding conditions on Mauna Loa, Hawaii, see the Methods section; cloud base precipitation rates (right axis) estimated from CloudSat satellite (mean for October/November 2006-2009 between 22°S and 18°S, red shading showing 1:30am and 1:30pm local time overpasses) and from the VOCALS-REx field experiment (black and blue squares from aircraft radar and in-situ precipitation probes respectively, in the latitude range 18-22°S); **(b)** observed (solid circles: aircraft during VOCALS [*Bretherton et al.* 2010, *Wood et al.* 2011], diamonds: satellite estimates from MODIS, 18-22°S) and modeled mean cloud droplet concentration N_d for different model scenarios as denoted in legend and discussed in the text.

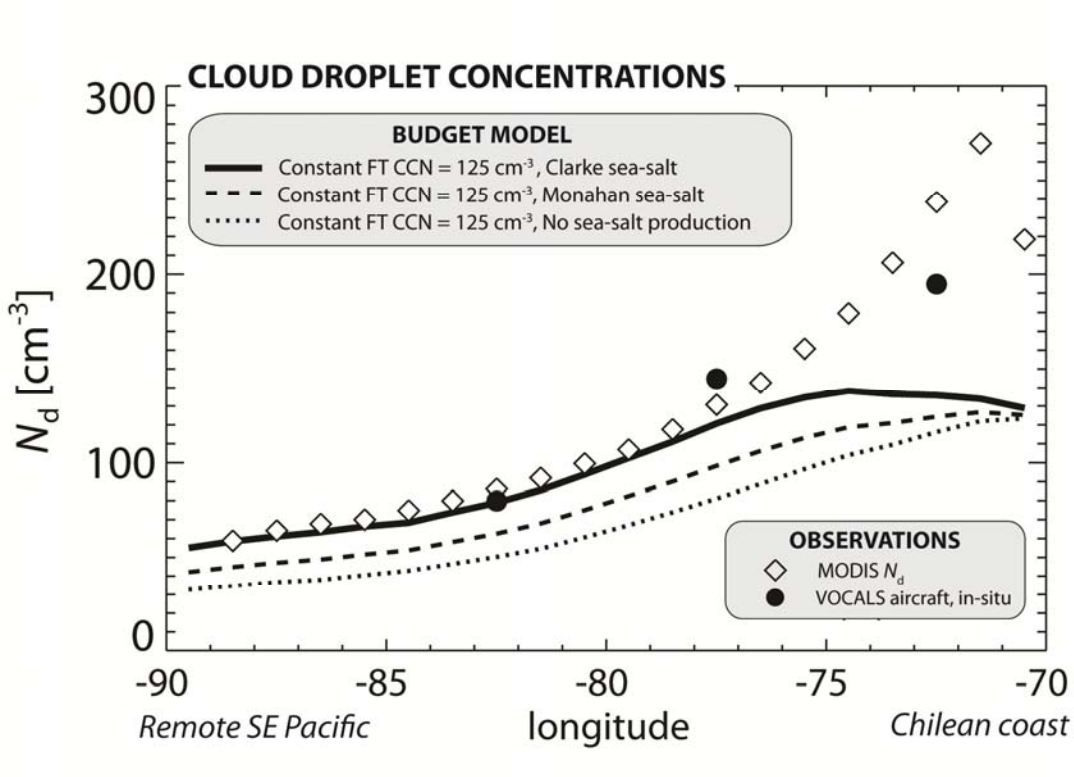

Figure 3: Effects of different assumptions regarding primary production of sea-salt in the model. Same as Fig. 2b, but showing sensitivity to sea-salt aerosol parameterization used. Observed (solid circles: aircraft during VOCALS [taken from *Bretherton et al.* 2010], diamonds: satellite estimates from MODIS, 18-22°S) and modeled mean cloud droplet concentration N_d. Solid line: standard model set up with constant FT CCN. Dashed line: Monahan sea-salt parameterization [*Monahan et al.* 1986] in place of *Clarke et al.* [2006]. Dotted line: No primary production of sea-salt at all.

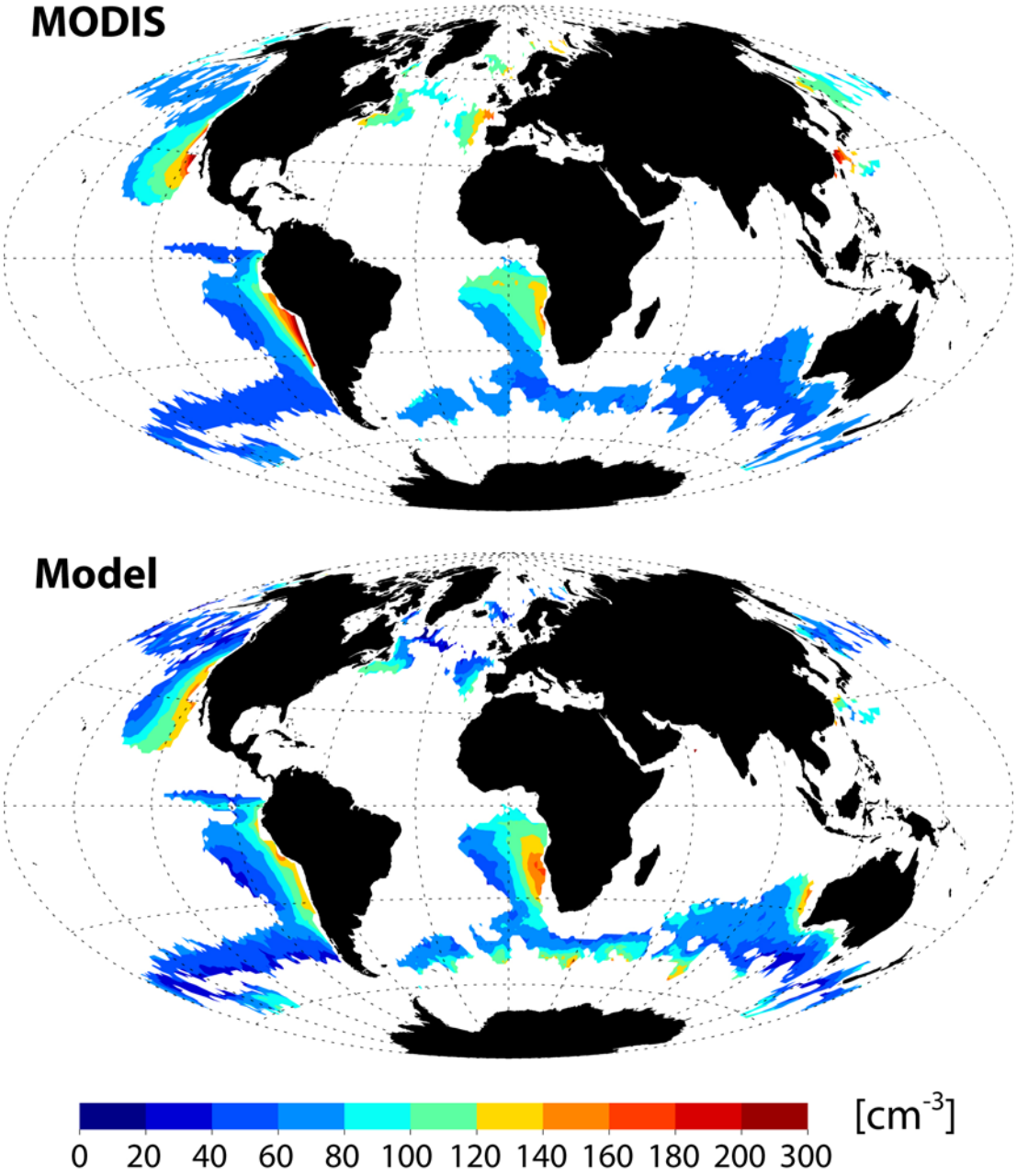

Figure 4: Cloud droplet concentrations in regions of extensive marine low clouds observed by satellite and from the budget model. Annual mean cloud droplet concentration N_d for extensive marine low clouds under conditions of large scale subsidence, (a) from MODIS (see section 3.5); (b) from the steady-state CCN budget model for the same regions.

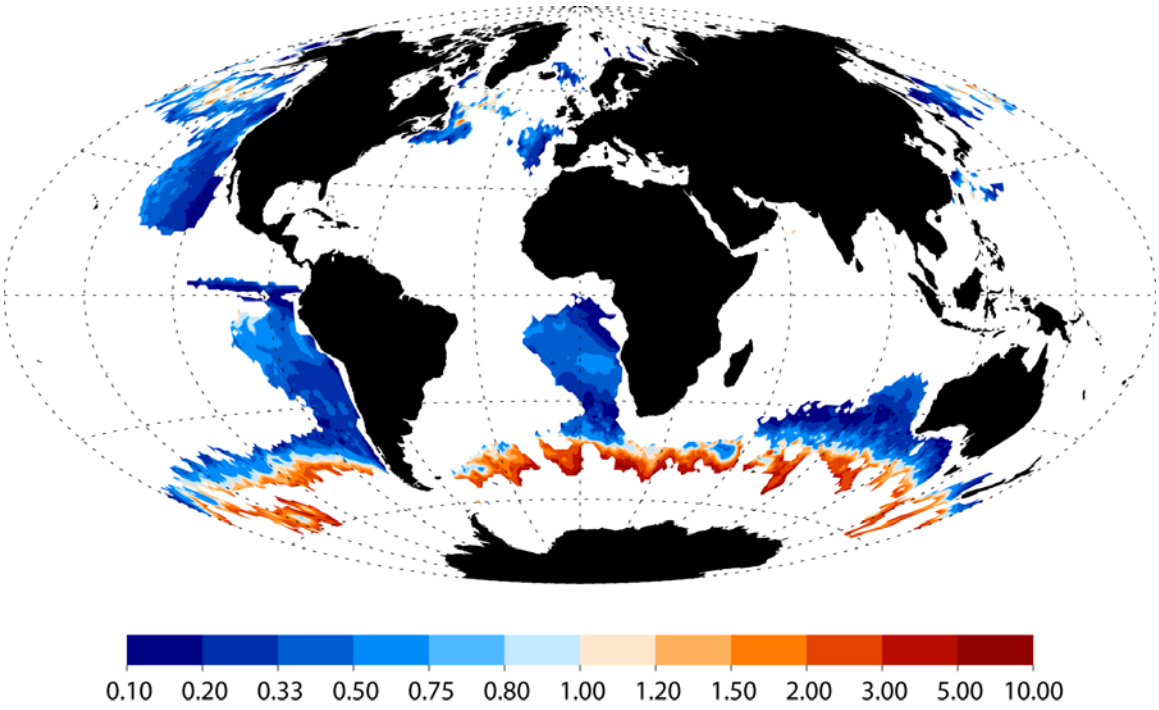

Figure 5: Ratio of CCN flux from surface to that from entrainment from the free troposphere (FT) in the model. The FT CCN concentration is set to 125 cm^{-3} and the surface source depends upon surface wind speed. In the subtropics and tropics, the majority of the CCN originate from the FT, but in the midlatitudes where winds are stronger, the surface source can exceed that from the FT.

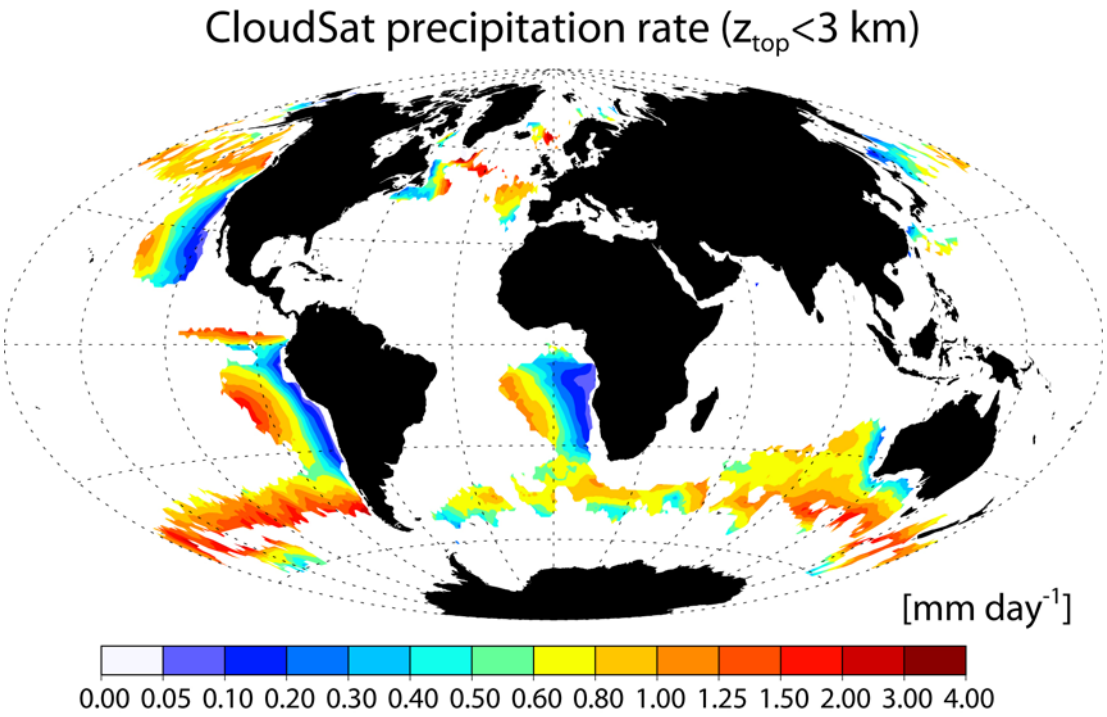

Figure 6: Mean precipitation rate at cloud base from low clouds (cloud top height z_{top}<3 km) estimated with spaceborne radar measurements from CloudSat [Lebsock and L'Ecuyer 2011]**.** Data are screened to display regions of extensive marine low clouds under conditions of mean subsidence as in Fig. 4.

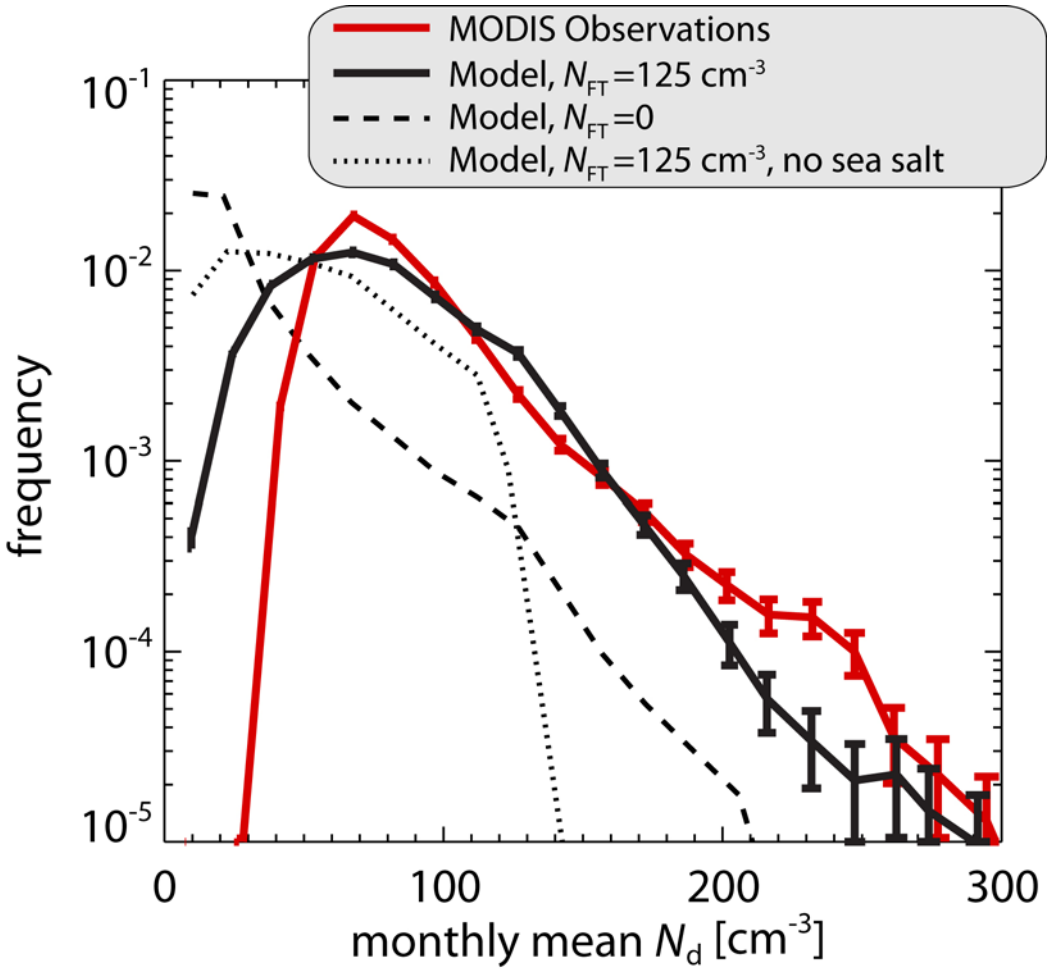

Figure 7: Frequency distributions of observed and modeled monthly mean cloud droplet concentration. Only months that meet the criteria needed to contribute to the means shown in Fig. 4 (regions with extensive low clouds under divergent conditions) are shown. Shown here are the base version of the model (i.e. that used to construct Fig. 4, solid black), together with estimates with no FT contribution to CCN (dashed), and no sea salt contribution (dotted). Error bars show the 95% confidence interval in the frequency estimates for the observations and for the model base case due to sampling limitations.

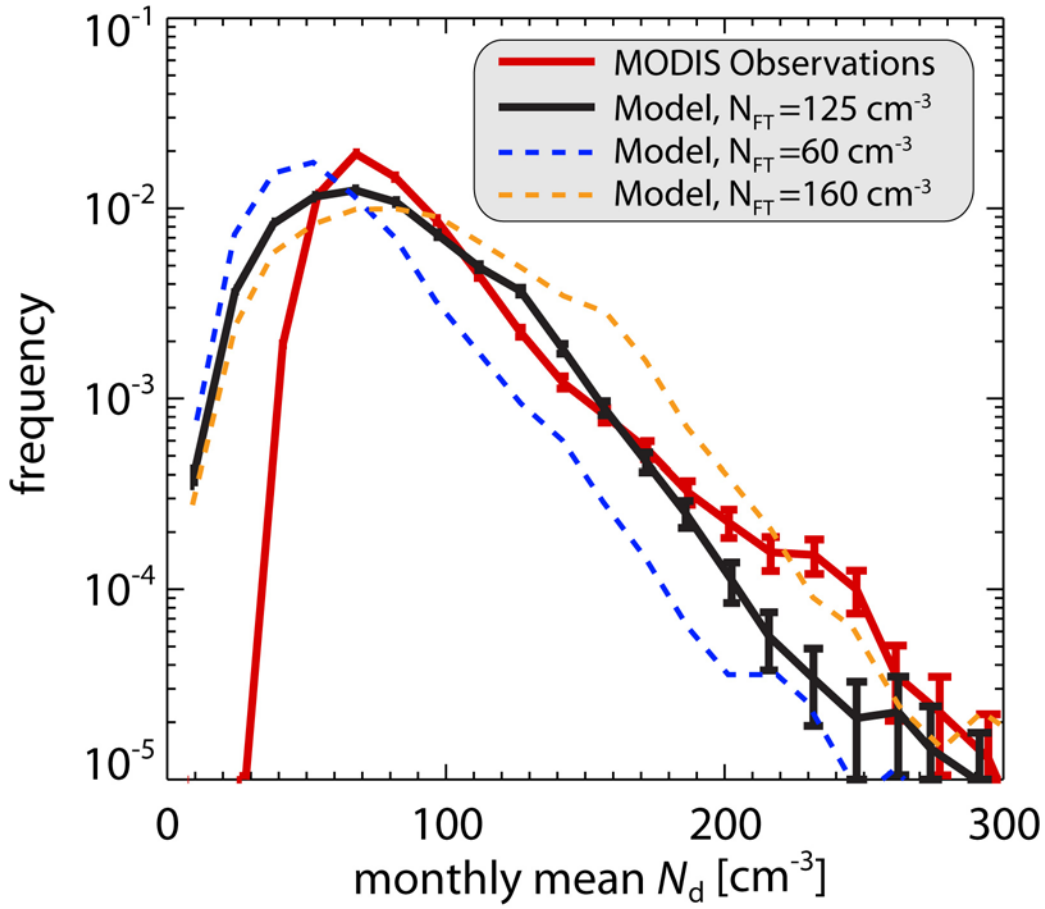

Figure 8: Sensitivity to assumed free tropospheric CCN concentration N_{FT} of the frequency distributions modeled monthly mean cloud droplet concentration. Only months that meet the criteria needed to contribute to the means shown in Fig. 4 (regions with extensive low clouds under divergent conditions) are shown. Shown here are the base version of the model (i.e. that used to construct Fig. 4, solid black), together with model estimates with low (N_{FT} = 80 cm^{-3}) and high (N_{FT} = 160 cm^{-3}) estimates of the FT contribution to CCN (dashed blue and orange respectively). Error bars show the 95% confidence interval in the frequency estimates for the observations and for the model base case due to sampling limitations.